Lattice-Compliant Simulations of Anti-Ferromagnetic Textures and their Response to Spin-Orbit Torques

Jacques Miltat, André Thiaville

Lattice-Compliant Simulations of Anti-Ferromagnetic Textures and their Response to Spin-Orbit Torques

Jacques Miltat* and André Thiaville
Université Paris-Saclay, CNRS, Laboratoire de Physique des Solides, 91405, Orsay, France
(Dated: December 24, 2021)

Spin textures in perfectly ordered antiferromagnetic ultra-thin films are evaluated on the basis of atomistic simulations and compared to the results of recent extensions of the $(\mathbf{l}, \mathbf{m})$ decomposition model. A comparison between similar textures supported by either a *bcc* or a *fcc* lattice shows that the sole inclusion of symmetric Heisenberg exchange interactions suffices to provide, when geometry commands, a natural canting between neighboring $\mathbf{s}_\uparrow$ and $\mathbf{s}_\downarrow$ spins within a texture. Moreover, a pure 'at lattice points' dipole model leads to natural symmetries in clear disagreement with expectations from the $(\mathbf{l}, \mathbf{m})$ model. Inversely, properties such as wall mobility under spin orbit torques depending mostly on wall geometrical characteristics such as chirality and chirality axis orientation prove, as anticipated, primarily lattice immune.

I. INTRODUCTION

C. Kittel and F. Keffer's analysis of antiferromagnetic resonance [1, 2], revealed i) the existence of a resonance frequency in zero field, ii) the coexistence of several resonance modes, all with large frequencies w.r.t. the ferromagnetic case. These concepts, established in a two spin-lattices approach, have received a full experimental confirmation in the case of e.g. MnF_2 [3, 4], NiO [5, 6] or $CrCl_3$ [7]. Large frequencies, in the TeraHz range, due to precession around the sum of the exchange and anisotropy fields, the latter potentially incorporating dipole-dipole interactions, entail large domain wall velocities at low damping. Unusual wall velocities, up to 20 km/sec, have indeed been experimentally observed in rare-earth orthoferrites, not exactly antiferromagnets though, but weak ferromagnets as early as 1978 (see [8]). Recently, a possible electrical control of the order parameter in antiferromagnets with potential applications to spintronics has attracted a sustained interest both in metallic [9–16] and insulating antiferromagnetic compounds [17–21].

In ferromagnets (F), micromagnetic simulations have more than often proved instrumental in deciphering responses of small ferromagnetic elements to fields or to spin transfer torques (STT), both in the frequency and time domains. In antiferromagnets (AF), the sole fact that spin-orbit torques (SOT) may reverse at the atomic scale [9, 22] ought to promote atomistic simulations of the spin dynamics. Such codes exist, e.g. [23–26]. However, although numerous applications of atomistic codes may be traced back in the case of F's, fewer examples deal with AF's [26–29] beyond the 1D spin chain limit [30–32]. The spin orientation in AF's is characterized by the superposition of spatially fast variables (spin inversion on adjacent sites) and slow variables (e.g. in the presence of an AF texture). Efforts to separate the fast from the slow variables start with the $(\mathbf{l}, \mathbf{m})$ and Haldane's decompositions [33–35]. Haldane's decomposition retains a general staggered field character for the transverse spin component. In the words of Tveten *et al.*[36], Haldane's canting field represents the dynamic magnetization induced by temporal variations of the order parameter. The $(\mathbf{l}, \mathbf{m})$ decomposition, $\mathbf{l} = \frac{1}{2}(\hat{\mathbf{s}}_\uparrow - \hat{\mathbf{s}}_\downarrow), \mathbf{m} = \frac{1}{2}(\hat{\mathbf{s}}_\uparrow + \hat{\mathbf{s}}_\downarrow)$ allows to envisage the new variables $\mathbf{l}$ and $\mathbf{m}$ as continuous variables. Models using the $(\mathbf{l}, \mathbf{m})$ decomposition implicitly assume, however, $\mathbf{l}$, the so-called Néel vector, and $\mathbf{m}$, the magnetization, to be located at the *same node* within a regular mesh in spite of the initial need to associate two specific AF coupled spins with *distinct locations* within the primary lattice. As a consequence, Papanicolaou [30] is lead, in his mesoscale treatment of 1D textures, to introduce asymmetrical exchange interactions in order to allow for some canting within a texture (a wall in this case) between neighbouring $\mathbf{s}_\uparrow$ and $\mathbf{s}_\downarrow$ spins. An extension to the 3D case [36] appears, however, questionable since tantamount to the introduction of isotropic asymmetric exchange interactions where none such exist apart from surface and/or interface Dzyaloshinskii-Moriya (DM) interactions.

In this work, we analyze characteristic spin textures in AF thin films within an atomistic model focusing on two crystal structures, the *bcc* and the *fcc* cubic Bravais lattices, and provide values for their energy, concentrating in a first step on the exchange and anisotropy energies. In a second step, the introduction of dipole-dipole interactions allows to quantify their role in the stability of the AF order and the generation of (minute) stray fields above a free surface. We examine next the conditions in which the numerical computation load may be alleviated *via* what we term "lattice inflation" or "swelling". Lastly, we analyse the role of spin-orbit torques on specific textures in the presence of DM interactions (see [22, 37]).

II. ATOMISTIC MODEL

The atomistic model Hamiltonian includes Heisenberg exchange interactions, anisotropy, the Zeeman and dipole-dipole interactions energies as well as

* jacques.miltat@universite-paris-saclay.fr

Dzyaloshinskii-Moriya interactions:

$$\begin{aligned}
\mathcal{H} &= \mathcal{H}_{\rm Exch} + \mathcal{H}_{\rm K} + \mathcal{H}_{\rm Ha} + \mathcal{H}_{\rm Dip} + \mathcal{H}_{\rm DMI} \\
\mathcal{H}_{\rm Exch} &= -\frac{1}{2}\sum_{i\neq j} J_{ij}\,(\hat{\mathbf{s}}_i \cdot \hat{\mathbf{s}}_j) \\
\mathcal{H}_{\rm K} &= k_1 \sum_i f(s_{i,x}^2, s_{i,y}^2, s_{i,z}^2) + k_2 .... \\
\mathcal{H}_{\rm Ha} &= -\mu_{\rm s} \sum_i (\mathbf{B}_{\rm a} \cdot \hat{\mathbf{s}}_i) \\
\mathcal{H}_{\rm Dip} &= -\frac{1}{2}\mu_{\rm s} \sum_i (\mathbf{B}^i_{\rm Dip} \cdot \hat{\mathbf{s}}_i) \\
\mathcal{H}_{\rm DMI} &= \frac{1}{2}\sum_{i\neq j} \mathbf{D}_{ij} \cdot (\hat{\mathbf{s}}_i \times \hat{\mathbf{s}}_j)
\end{aligned} \tag{1}$$

where, $\hat{\mathbf{s}}_i$ is a unit vector collinear with the local moment, index i. $\mathbf{B}_{\rm a}$ and $\mathbf{B}_{\rm Dip}$ are the applied and dipole field, respectively. The anisotropy constants k are expressed in terms of an energy whereas $J_{ij}(F > 0; AF < 0)$ is defined as an energy per bond, hence the factor $\frac{1}{2}$ in front of the exchange energy. We choose here the meV as the energy unit and express all fields $\mathbf{B}$ in Tesla (T), or fraction thereof, whereas $\mu_{\rm s}$ is expressed in Bohr magneton translated into an energy per T ($1\ \mu_{\rm B} \approx 5.8\ 10^{-2}$ meV.T^{-1}). Lastly, $\mathbf{D}_{ij}$ is the Dzyaloshinskii vector, $\mathbf{D}_{ij} = d_{\rm DMI}(\hat{\mathbf{u}}_{ij} \times \hat{\mathbf{z}})$ in the case of interface driven DM interactions with the highest symmetry, $\hat{\mathbf{u}}_{ij}$ is the unit vector along the line joining sites i and j in the surface plane and $\hat{\mathbf{z}}$ the normal to the surface. $d_{\rm DMI}$ is also defined as an energy per bond.

The equation of motion is an exact analog to the Landau-Lifshitz-Gilbert (LLG) equation of magnetization motion within micromagnetics, namely,

$$\frac{d\hat{\mathbf{s}}}{dt} = -\gamma(\hat{\mathbf{s}} \times \mathbf{B}_{\rm Eff}) + \alpha\gamma\left[\hat{\mathbf{s}} \times \frac{d\hat{\mathbf{s}}}{dt}\right] + \tau_{\rm SOT} \tag{2}$$

where, γ is the gyromagnetic ratio, α the damping parameter, $\tau_{\rm SOT}$ the spin-orbit torque and $\mathbf{B}_{\rm Eff}$, the effective field that, classically, reads:

$$\mathbf{B}_{\rm Eff} = -\frac{1}{\mu_S}\frac{\delta\mathcal{H}}{\delta\hat{\mathbf{s}}} \tag{3}$$

In these equations, both the exchange field and the dipole field mirror the lattice symmetries.

We consider here two simple cubic lattices, the *bcc* and the *fcc* lattices, with as background antiferromagnetic materials Cr on the one hand and NiO on the other. Chromium has been widely studied at the time of the discovery of the Giant Magnetoresistance [39, 40] and, later, in the context of exchange coupling. In their study of 3*d* transition metal monolayers on various (001) surfaces, including Ag, Au and Pd, Blügel *et al.* [41, 42] envisage two possibilities for a Cr overlayer: either a F $p(1\times1)$ or an AF $c(2\times2)$ spin ordering and conclude that both are stable with, however, a slightly lower energy for the AF ordering. On the other hand, as soon as the thickness of a free standing layer exceeds 3 monolayers, the staggered stacking of F (001) planes becomes more stable. A largely amplified moment at the interface has been obtained from *ab initio* calculations; it also appears that Cr layers thin enough are devoid of incommensurate spin density waves (see [43] for a timely review). High quality Cr layers have also been grown on W [44]. For bulk Cr, the spin orientation is in-plane with preferred directions along [100] and [010] in the (001) plane. We adopt this general view, without, however, imposing an exalted moment at the interface. In the *bcc* lattice, each $\uparrow$ spin has 8 $\downarrow$ nearest neighbours (n.n.) and *vice versa*, as recalled in Fig. 1. The exchange field limited to n.n. for a site with its full environment thus reads:

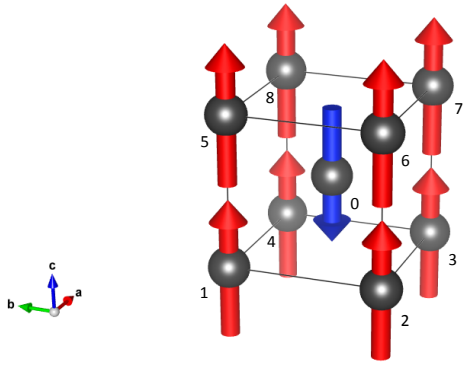

FIG. 1. *bcc* environment : A $\downarrow$ spin has 4 $\uparrow$ nearest neighbours in the (001) plane below, 4 in the (001) plane above. The vertical (**c**) axis in the figure coincides with the [001] direction. Spin orientation owing to the sole legibility. Figure drawn with VESTA [38].

$$bcc: \mathbf{B}^i_{\rm Exch} = +\frac{1}{\mu_S}\sum_{j=1,N(=8)} J_{ij}\,\hat{\mathbf{s}}_j \tag{4}$$

According to Eqn.4, the exchange effective field aligns spin i with minus the average spin orientation of its 8 n.n.($J_{ij} < 0$). This sole mechanism allows for the lattice induced canting of n.n. spins within a texture as shown below (Section III). We also adopt a uniform value for the Cr moment, a symbolic value $\mu_S = 1\mu_B$, somewhat exceeding the value stemming from first principle calculations. We retain a value of -15 meV for the exchange energy per link, in agreement with [45].

Various forms of anisotropy have been used, with for the *bcc* lattice, for instance, the cubic anisotropy ($K_{cc} f(\alpha^2, \beta^2, \gamma^2)$) and a general orthorhombic anisotropy reading $K_u \cos^2\theta + K_{iP} \sin^4\theta \cos^2(2\phi)$, where α, β, γ are the director cosines of the spin orientation in the cubic axes, θ and ϕ the polar and azimuthal angle of the spin orientation owing to the specific orientation of the computation box. The exact form of the anisotropy will be made explicit with each computation result below.

NiO is another well-studied AF material, sharing the

structure of MnO, the first synthesized antiferromagnetic oxide [46]. In the search for high quality supported NiO or CoO films, Ag(001) and MgO have played a leading role due to their minute lattice parameter mismatch [19, 20, 47–50]. NiO growth has, however, also been achieved with $SrTiO_3$ as a substrate [18] as well as Pt(111) [17]. Several first principles studies of magnetic oxides appeared during the last decade [51–53]. Only one of them [51] evoques a possible reduction of the Ni moment for the first grown layer over Ag(001). All agree on the AF2 spin ordering within NiO or CoO, meaning staggered F (111) planes, and on the existence of exchange interactions with nearest neighbours (n.n.), at distance $a/\sqrt{2}$, and next nearest neighbours (n.n.n.), at distance a, corresponding, respectively to 90° and 180° (Ni^{2+}–O^{2-}– Ni^{2+}) bonds. Values obtained for the exchange energies J_1 (n.n.) and J_2 (n.n.n.), however, somewhat fluctuate. We consider here perfect (111) NiO epilayers and adopt the exchange parameters provided long ago by neutron scattering techniques [54], namely $J_1 = +1.39$ and $+1.35$ meV for (ferromagnetic) n.n. interactions within the (111) plane and (ferromagnetic) n.n. interactions out-of-plane, respectively, and $J_2 = -19.05$ meV for (antiferromagnetic) n.n.n. interactions (see Fig. 2). With 6 n.n. in-plane, 6 n.n. out-of-plane, and 6 n.n.n. for a site with its full environment, the exchange field reads:

$$fcc : \mathbf{B}^i_{\rm Exch} = +\frac{J_1^{iP}}{\mu_S}\sum_{j=1,6}(\hat{\mathbf{s}}_j^{iP}) + \frac{J_1^{ooP}}{\mu_S}\sum_{j=1,6}(\hat{\mathbf{s}}_j^{ooP}) + \frac{J_2}{\mu_S}\sum_{j=1,6}(\hat{\mathbf{s}}_j) \quad (5)$$

where, iP and ooP stand for in-plane and out-of-plane, respectively. Due to the AF2 character of antiferromagnetism in NiO, ooP n.n. exchange interactions are frustrated.

We also adopt a uniform value for the Ni^{++} moment, a symbolic value $\mu_S = 2\mu_B$, only marginally exceeding values obtained from first principles calculations. Anisotropy is dealt with on the same footing as in the Cr case, namely a generalized orthorhombic anisotropy reading $K_u \cos^2\theta + K_{iP}\sin^6\theta\cos^2(3\phi)$ in order to keep track with the six-fold anisotropy in the (111) plane.

Numerical simulations below have all been performed by means of in-house codes ported to graphical processing units (GPU's). Epilayers contain 16 and 12 atomic layers in the *bcc* (interlayer spacing: $a/2$) and *fcc* (interlayer spacing $a\sqrt{3}/3$)lattices, respectively, where a is the cubic cell parameter. Double precision has been used throughout.

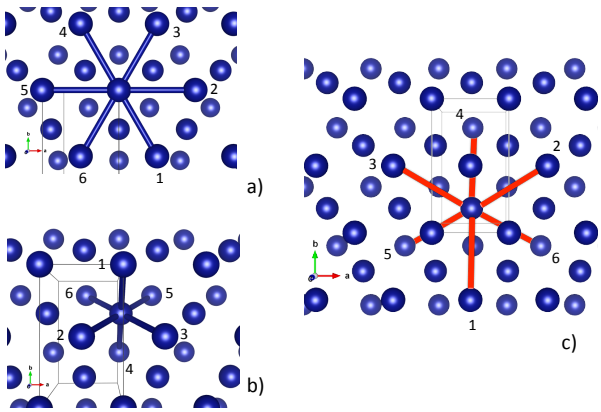

FIG. 2. *fcc* environment : Top perspective view of Ni ions belonging to 3 successive (111) planes (depth indicated by the atoms size). The **c** axis is normal to the plane of the figure and coincides with the [111] direction. a) For any given Ni ion within a given (111) plane, there exist 6 nearest neighbours (n.n.) in plane; b) n.n. arrangement around a given Ni ion one (111) plane up, one plane down; c) *Ibid* for next nearest neighbours (n.n.n.). Figures generated with VESTA [38].

III. NÉEL (BEND) AND HEAD-TO-HEAD (SPLAY) WALLS

We consider in this section two types of walls in AF systems where the prevailing anisotropy tends to maintain spins in-plane with respect to the geometry of the slab, namely Néel and Head-to-Head (resp. Tail-to-Tail) walls that, in the terminology used in nematic liquid crystals, may be termed Bend and Splay walls [55]. At this stage, only the exchange and anisotropy terms in the Hamiltonian are being considered. In the absence of dipole fields, such walls are anticipated to entail equivalent energies.

A. *bcc* Spin lattice

Specifically, in the axes of Fig. 3, the anisotropy energy now reads:

$$E_k = k_u s_z^2 + k_{iP}(s_x^2 - s_y^2)^2 \quad (6)$$

with k_u and $k_{iP} > 0$. We adopt also here symbolic values for the anisotropy constants, namely $k_u = 0.1$ meV, $k_{iP} = 0.05$ meV. Under such conditions, spins remain in the (001) plane and rotate gradually from the [100] to the [010] easy axis as the result of the competition between exchange interactions and anisotropy (see Fig. 3) [56]. The global AF ordering between successive (001) planes is, however, preserved. Similar remarks apply to the Splay wall spin texture displayed in Fig.4. The Bend and Splay 90° wall profiles displayed in Fig.5, prove essentially similar, as anticipated. The roles of the s_x and s_y spin components are simply swapped. The lattice geometry commands an offset between the spin locations

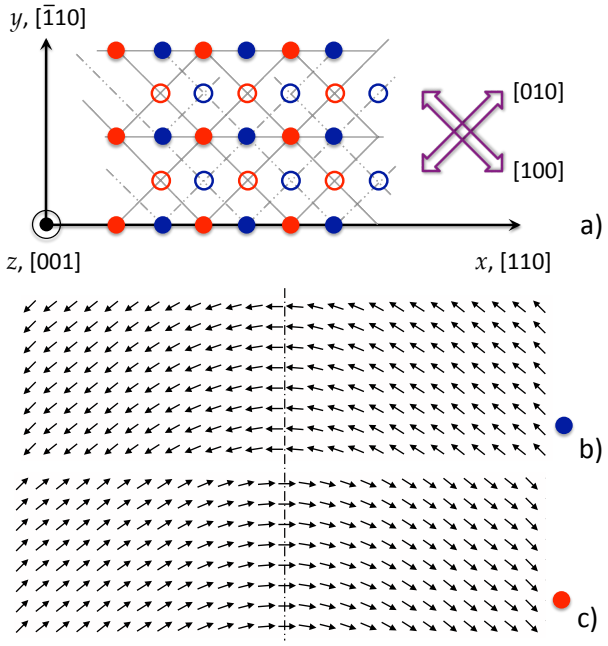

FIG. 3. AF Néel wall in a *bcc* spin lattice. The [001] direction is normal to the plane of the figure and all spins tend to belong to the easy (001) plane where the easy directions are the cubic axes. The spin texture is displayed around the mid-plane of a 16 monolayer (ML) stack (≈ 2.3 nm thick), one (001) plane with $\uparrow$ spins (c), one plane above with $\downarrow$ spins (b). a) Spin location projection onto the (001) plane and axes definition. Only the spins belonging to rows with full symbols in a) are represented, *i.e.* one half of the spins, where red, blue symbols correspond to $\uparrow$ and $\downarrow$ spins, respectively. The relative shift between b) and c) reflects the symmetry properties of the *bcc* lattice. Distance between two spins, along x or y: $a\sqrt{2}$, where a is the lattice parameter.

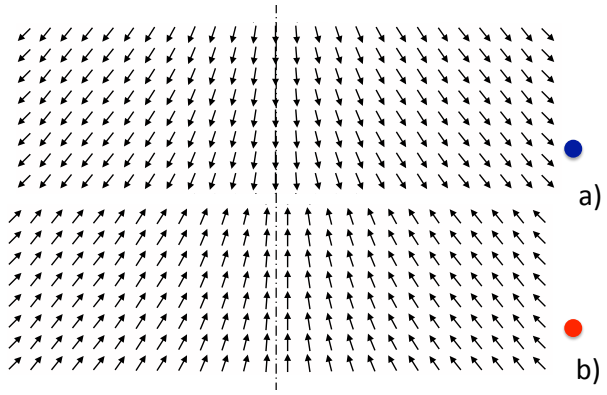

FIG. 4. AF Splay wall in a *bcc* spin lattice. a) $\downarrow$ spins plane, b) $\uparrow$ spins plane. Same representation conventions as in Fig.3.

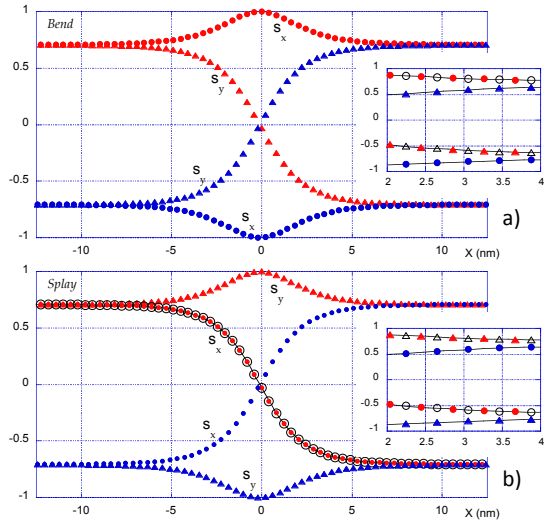

FIG. 5. *bcc* spin lattice: a) Néel (Bend) and b) Splay wall profiles corresponding to Figs.3 and 4, respectively. The large open symbols in b) correspond to a fit by a classical Bloch wall profile. Insets: superposition of $-s_{x,y}$, $\downarrow$ plane (open symbols) and $s_{x,y}$, $\uparrow$ plane (full symbols).

along equivalent rows located in adjacent (001) planes, as captured in Fig. 3,a. Plotting minus s_x and s_y of the $\downarrow$ plane along the spin components of the $\uparrow$ plane, or *vice versa*, clearly reveals the continuous character of the spin rotation across the two sub-lattices, or, equivalently, the continuous spin-canting between AF coupled neighbouring spins within a texture (see the insets in Fig.5).

Before addressing the wall energy issue, it is worth identifying what may be attributed to the texture (curvature) within the exchange energy. Looking back at Eqn.1, any uniform orientation of the order parameter yields for the *bcc* lattice an energy $4\,J_{ij} < 0$ *per* general site. Therefore the wall contribution to the exchange energy is $-\frac{1}{2}J_{ij}\sum_i(\sum_{j=1,N}(\hat{\mathbf{s}}_i\cdot\hat{\mathbf{s}}_j)+N)$, where N is the number of n.n., $N=8$ for a spin with its full environment within a *bcc* lattice.

With this in mind, the wall exchange and anisotropy energies are found to be almost strictly equal, namely 872.393 meV and 871.078 meV, respectively, for a $L\times t$ wall surface, where L is the wall length and t the slab thickness, namely $(130\ a\sqrt{2}/2)\times(16\ a/2)$ for this computation. Note that the volume over which the wall energy is computed represents only a fraction of the computation volume in order to minimize edge effects. With $a = 0.2884$ nm (Cr), the wall energy amounts to $\approx$ 28.504 meV/nm^2. The Splay wall profile s_x in Fig.5,b has been fitted with a function characteristic of a Bloch wall in a ferromagnet. The excellent fit provides a precise value for the width parameter of that model Bloch wall, namely $\Delta^* = 1.713$ nm. Wall width combined with energy provide effective values for the continuum limit of the exchange and anisotropy constants, respectively $A^* = 12.207$ meV/nm and $K_{iP} = 4.160$ meV/nm^3. The discussion of such estimates is deferred to the end of the section.

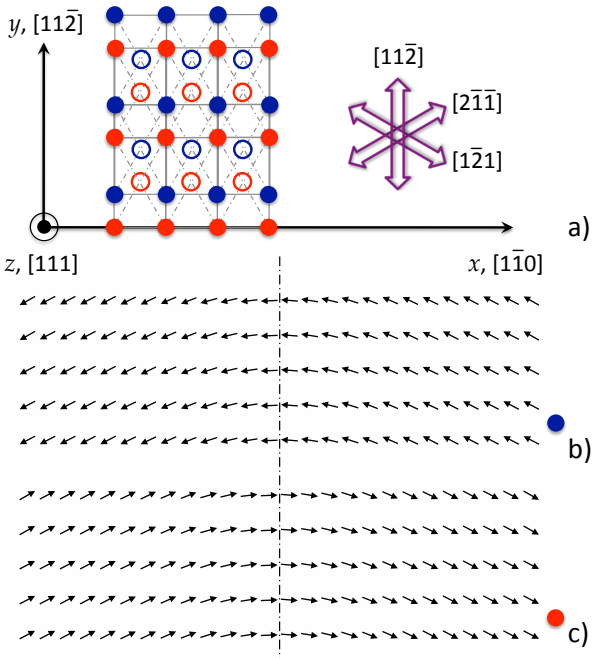

FIG. 6. AF Néel (Bend) wall in a *fcc* spin lattice. The [111] direction is normal to the plane of the figure and all spins belong to the easy (111) plane where the easy directions are the $\langle\bar{2}11\rangle$ directions in the (111) plane. The spin texture is displayed around the mid-plane of a 12 monolayer (ML) stack ($\approx$ 3 nm thick), one (111) plane with $\uparrow$ spins (c), one plane above with $\downarrow$ spins (b). a) Spin location projected onto the (111) plane and axes definition. In agreement with the geometry of the AF unit cell, only the spins located at positions labeled with full symbols in a) are represented in b) and c), where full red, blue symbols correspond to $\uparrow$ and $\downarrow$ spins, respectively. Here, the shift between b) and c) takes place along the y directions and amounts to $d_{\rm nn}\sqrt{3}/3$, where $d_{\rm nn}$ is the distance between nearest neighbours. Distances between two spins in the representation: $d_{\rm nn}$ and $d_{\rm nn}\sqrt{3}$, along x and y, respectively.

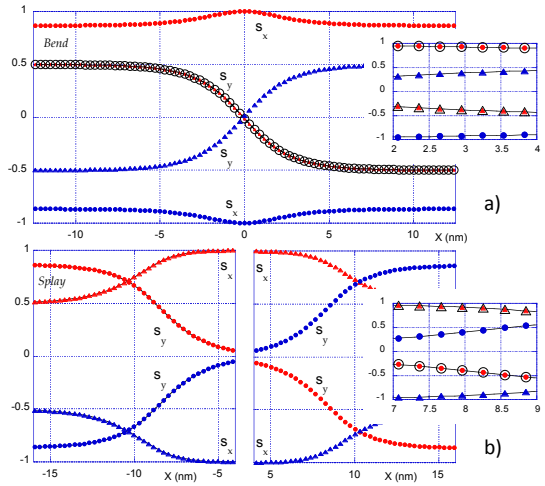

FIG. 7. *fcc* spin lattice: a) Néel (Bend) wall profile corresponding to Fig.6 and b) decomposed Splay wall profile. The large open symbols in a) correspond to a fit by a classical Bloch wall profile. Insets: *Ibid* Fig.5.

B. *fcc* Spin lattice

We solely consider below walls separating S(or Spin)-domains, i.e. domains belonging to a single T(or Twin)-domain [57, 58]. A T-domain is characterized by a unique {111} AF2 ordering. Four T-domains may coexist, corresponding to (111), $(\bar{1}11)$, $(1\bar{1}1)$ or $(11\bar{1})$ F-ordered planes, respectively. In the axes of Fig. 6, the anisotropy energy may be expressed as:

$$E_k = k_u s_z^2 + k_{iP}\ s_x^2(s_x^2 - 3s_y^2)^2 \qquad (7)$$

Adopting here also symbolic values for the anisotropy constants, namely $k_u = 0.1$ meV, $k_{iP} = 0.05$ meV [59], spins remain confined to the (111) plane and rotate gradually from the $[2\bar{1}\bar{1}]$ to the $[1\bar{2}1]$ easy axis, resulting in a 60° Néel wall (see Fig.6). Due to a specific distribution of the easy axes (6-fold symmetry), the equivalent Splay wall decomposes spontaneously into two 60° Splay walls with the same handedness as shown by the wall profiles in Fig.7.

In full similarity with the *bcc* case, the Néel wall profile may be fitted by a pure Bloch wall profile as displayed in Fig.7. In contradistinction to the *bcc* case, however, no canting exists between equivalent spins belonging to two successive (111) planes as shown in the insets of Fig.7. Had we, however, considered a Néel wall parallel to the $(11\bar{2})$ plane, then spin canting between AF coupled neighbouring spins would have been recovered.

The contribution of exchange interactions to the wall energy proves more complex than in the *bcc* case due to the existence of frustrated n.n. interactions. However, when limiting the evaluation of the exchange energy to n.n.n. interactions, the expression derived in the *bcc* case remains valid with $J_{ij} = J_2$ and $N = 6$. The recorded exchange and anisotropy energies amount to 586.198 meV and 609.352 meV, respectively. With a global thickness close to 2.9 nm, a lattice parameter $a = 0.41705$ nm, and consequently, $d_{\rm nn} = a\sqrt{2}/2 = 0.2949$ nm, $d_{\rm nnn} = d_{\rm nn}\sqrt{2} = a$, the 60° Néel wall energy amounts to 20.254 meV/nm^2 whereas the wall profile fit yields an effective wall width parameter equal to $\Delta^* = 1.8814$ nm. Wall width combined with energy provide effective values for the continuum limit of the exchange and anisotropy constants, respectively $A^* = 9.540$ meV/nm and $K_{iP} = 2.687$ meV/nm^3.

C. Wall width and energy analysis

We have dealt above with 90° and 60° Néel walls in a *bcc* and a *fcc* lattice, respectively. It is straightforward to show that, due to a prevailing uniaxial anisotropy, spins are confined to their respective easy planes, namely

the (001) and the (111) plane. The anisotropy energy may thus be reduced to $k_{iP}\sin^2 2\phi$ in the *bcc* case and $k_{iP}\sin^2 3\phi$ for the *fcc* lattice. Defining A and K as the exchange and anisotropy constants in the continuum limit, the energy density of these walls may be written as $\varepsilon = A\,(d\phi/dx)^2 + K\sin^2 2\phi$ or $\varepsilon = A\,(d\phi/dx)^2 + K\sin^2 3\phi$ owing to lattice, or, globally as $\varepsilon = A^*\,(du/dx)^2 + K\sin^2 u$, where $u = 2\phi$, $A^* = A/4$ in the *bcc* case, $u = 3\phi$, $A^* = A/9$ in the *fcc* case. The energy density expression in u entails a Bloch-type 180° wall with width parameter $\Delta^* = \sqrt{A^*/K}$ and energy $4\sqrt{A^*K}$.

The migration from a discrete spin system to a continuum is, in the ferromagnetic case, done classically as follows. Choosing here, as an example, the *bcc* lattice and referring back to the unit cell geometry depicted in Fig.1, a Taylor expansion up to the second order of spins $\mathbf{s}(\mathbf{r})$ located at the apices of the unit cell may be performed w.r.t. the spin at the cell centre, $\hat{\mathbf{s}}_0$, with, as a result, an exchange field reading:

$$\mathbf{B}^i_{\rm Exch} = \frac{J}{\mu_{\rm s}}\sum_{j=1,N}(\hat{\mathbf{s}}_j) = \frac{J}{\mu_{\rm s}}(N\hat{\mathbf{s}}_0 + a^2\nabla^2\hat{\mathbf{s}}|_0) \qquad (8)$$

The laplacian term at site 0 and $\hat{\mathbf{s}}_0$ are the only surviving terms in the Taylor expansion after summing-up over the 8 n.n.. The $\hat{\mathbf{s}}_0$ field component exerts no torque on $\hat{\mathbf{s}}_0$ itself and, thus, may, in the ferromagnetic case, be discarded. In the continuum limit, the exchange field reads $\mathbf{B}_{\rm Exch} = (2A/M_{\rm s})\nabla^2\mathbf{m}$, be it for the *bcc* or *fcc* lattice. Since $M_{\rm s}$, the saturation magnetization, is, for a *bcc* lattice, equal to $2\mu_{\rm s}/a^3$, one finds $A = J/a$, a still being the lattice cell parameter.

In order to treat the AF case on a similar footing, let us first consider a F spin chain (1D) embedding a wall. If ϵ is the angle between two adjacent spins, the contribution to the exchange energy of that spin pair is $-J_F cos(\epsilon)$. For constructing the equivalent AF spin chain, just revert one spin over two. The energy per spin pair becomes $-J_{AF}cos(\pi\pm\epsilon)$. In the spirit of Haldane [35], now define the order parameter as $\mathbf{l} = (-1)^i\mathbf{s}$, where i is the spin index along the chain. For any equivalent spin pair along the chain, the exchange energy is either $-J_{AF}cos(\pi\pm\epsilon)$, applying to $\mathbf{s}$, or $-|J_{AF}|cos(\epsilon)$, applying to $\mathbf{l}$. The argument is easily extended to 3D textures, with, as a particular example, $\mathbf{l} = (-1)^k\mathbf{s}$ in the case of the AF structures considered above, where k is the atomic layer index. The continuum limit values of the exchange and anisotropy constants remain therefore linked to their discrete counterparts as, *bcc* ($M_{\rm s} = 2\mu_{\rm s}/a^3$): $A = |J|/a$, $K = 2k/a^3$, *fcc* ($M_{\rm s} = 4\mu_{\rm s}/a^3$): $A = |2J|/a$, $K = 4k/a^3$.

From the fit of the wall profile and the wall energy computation, the following parameters were extracted, $A = 4A^* = 48.827$ meV/nm and $K = 4.160$ meV/nm^3 in the *bcc* case, $A = 9A^* = 85.860$ meV/nm and $K = 2.687$ meV/nm^3 in the *fcc* case, to be compared to *bcc*: 52.012 meV/nm and 4.169 meV/nm^3, *fcc*: 91.356 meV/nm and 2.757 meV/nm^3, respectively. It may be noticed that, perhaps unsurprisingly, the agreement between respective anisotropy values is better than between exchange parameters. Altogether, however, agreement is considered as satisfactory.

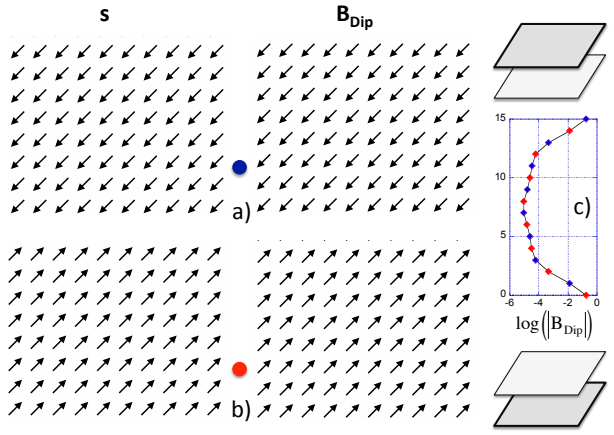

FIG. 8. *bcc* spin lattice: a,b) Uniform spin distribution ($s_x = s_y$, $s_z = 0$), left, and dipole field, right; a) Upper, b) Lower (001) plane. c) log of the dipole field modulus (T) across layer thickness.

IV. DIPOLE FIELDS

In their group theory analysis of dipolar crystals, Luttinger and Tisza [60, 61] first recall that the field at a point $\mathbf{r}$ due to a point-like dipole at the origin is linear in the dipole's moment $\mathbf{p}$, classically:

$$\mathbf{B}(\mathbf{r}) = \frac{\mu_0}{4\pi}\left(\frac{3(\mathbf{p}\cdot\mathbf{r})\mathbf{r}}{r^5} - \frac{\mathbf{p}}{r^3}\right) \qquad (9)$$

where $\mathbf{p} = \mu_{\rm s}\hat{\mathbf{s}}$. It ensues that the field displays the same symmetry as the generating dipole array. The dipolar energy then is a quadratic function of the dipoles vector components and finding the energy associated to various ordering modes ultimately reduces to an eigenvalue problem. It has been shown [60–62] that, for an infinitely extended *bcc* lattice, the dipole field is strictly zero at lattice points provided the dipoles are oriented along any of the cube axes. For a *fcc* lattice, with AF2 ordering (*i.e.* F-ordered {111} planes), the dipolar energy proves minimum for moments uniformly ordered in the {111} plane, irrespective of the spin orientation within the plane (see also [5]).

A. Uniform order parameter

Dealing with ultra-thin epilayers inherently leads to truncations in the dipole fields sums, hence a dipole contribution to the overall energy at variance from the bulk. We first evaluate the dipolar field lattice response when

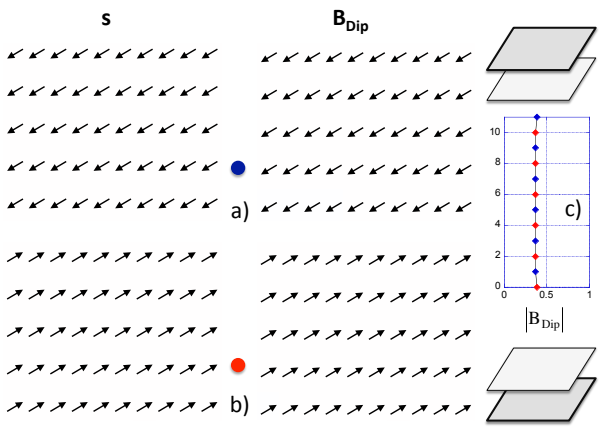

FIG. 9. *fcc* spin lattice: a,b) Uniform spin distribution ($|s_x| = \sqrt{3}/2$, $|s_y| = 1/2$, $s_z = 0$), left, and dipole field, right; a) Upper, b) Lower (111) plane. c) Dipole field modulus (T) across layer thickness.

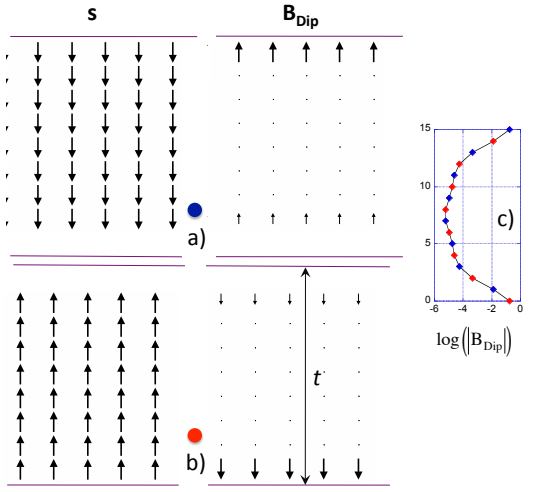

FIG. 10. *bcc* spin lattice: Uniform spin distribution ($s_x = s_y = 0$, $|s_z| = 1$), left, and dipole field, right, in a (x, z) plane cross section representation embedding the whole layer thickness t. a) is located one plane beneath b). c) Log of the dipole field modulus (T) across layer thickness.

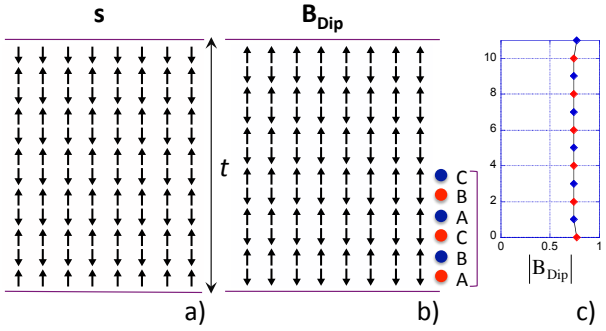

FIG. 11. *fcc* spin lattice: a) Projected spin distribution ($|s_z| = 1$) onto the $(11\bar{2})$ plane, and dipole field b) embedding the whole layer thickness t. c) Dipole field modulus (T) across layer thickness.

the order parameter is uniform, *i.e.* in the absence of any spin texture. Note that, in this context, the $(\mathbf{l}, \mathbf{m})$ decomposition assumes the system to be devoid of any field, assuming the $\mathbf{m}$ distribution to be the sole source of dipolar field. The main results may be summarized as follows: i) *bcc* lattice : for a spin direction along a $\langle 100 \rangle$ direction within the epilayer plane, the field decays rapidly from the outer surfaces, in agreement with the full 3D analysis of Luttinger and Tisza [60, 61]. A fairly large amplitude field however still subsists within the outmost atomic layers. The surviving field is dipole aligned (Fig.8), a property found to be independent of the spin orientation in the (001) plane; ii) *fcc* lattice : for a spin direction within the epilayer plane, (111) here, the dipole field is also, dipole oriented. In agreement with the 3D analysis [60, 61], the dipole field only weakly depends on the distance from outer surfaces (Fig.9). For all these cases, the dipole field stabilizes the spin orientation.

A different picture emerges when the dipoles are oriented along the epilayer normal. In the *bcc* lattice, a sizeable field is still to be found in the layers closest to the surfaces (Fig.10). The field is now, however, oriented opposite to the local moment and the field asymmetry between the bottom and the top surfaces is a consequence of the even number of atomic planes across the thickness, implying a spin orientation reversal between the outmost atomic layers. In the *fcc* lattice (Fig.11), the field is now also oriented opposite to the local spin, and its modulus increases gently only in the immediate vicinity of the surfaces. Thusly, for dipoles oriented along the epilayer normal, the dipole field acts for an ultra-thin AF epilayer as a local demagnetizing field.

It is clear that the dipolar energy reduces to a local anisotropy term when dealing with infinitely extended crystals. Is it the case, too, when dealing with ultra-thin epilayers ? It seems so since, both for the *bcc* or *fcc* lattices, dipolar interactions are consistent with the existence of an easy plane perpendicular to the epilayer normal. An anisotropy of the form $k_D s_z^2$ in the computation axes of Figs. 3,6 seems therefore adequate, provided k_D be a lattice specific function of the altitude z within the AF layer.

B. Spin Textures

Up to this point, we have only considered a uniform order parameter. Do the dipolar properties above remain true in the presence of a spin texture, as assumed, long ago, by Yamada [63, 64] in his study of walls in NiO ? Instead of attempting to answer globally to that question, we notice that the spin textures considered up to now are strictly planar. It follows that the z component of the dipole field is directly linked to the spin distribution

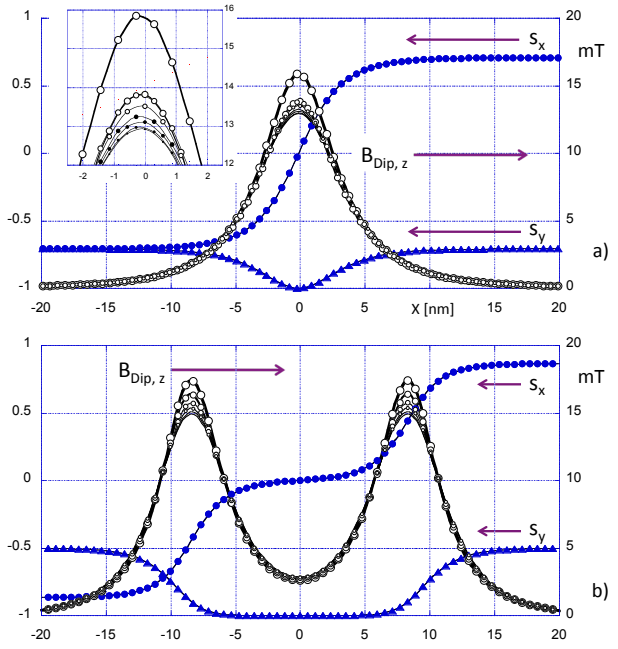

FIG. 12. Splay wall specific z dipole field component, a) *bcc*, b) *fcc* spin lattice, in layers n (top surface), $n-1, ..., n/2+1$ *vs* distance from wall center (nm). Decreasing symbol size with layer index (*cf* inset in a)). Left scale: spin components in the top atomic layer; right scale: z dipole field component (mT).

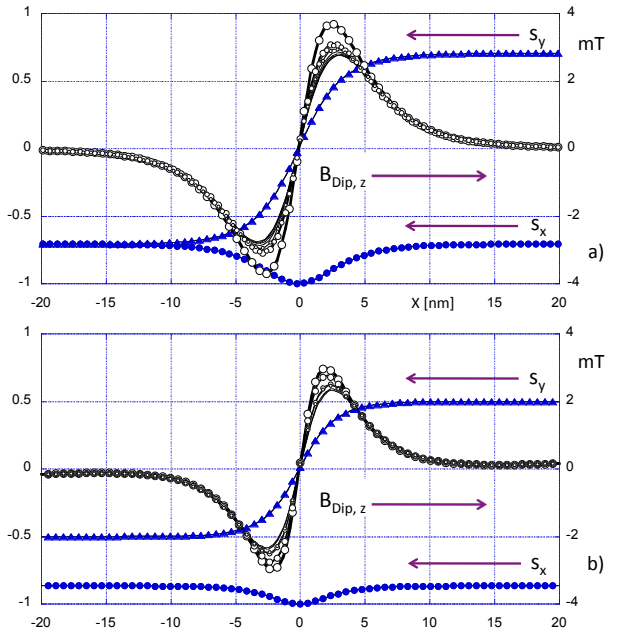

FIG. 13. Néel wall specific z dipole field component, a) *bcc*, b) *fcc* spin lattice, in layers n (top surface), $n-1, ..., n/2+1$ *vs* distance from wall center (nm). Decreasing symbol size with layer index. Left scale: spin components in the top atomic layer; right scale: z field component (mT).

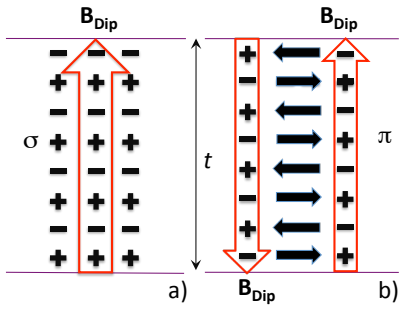

FIG. 14. Schematic magnetic charge distribution across a wall in successive atomic layers and resulting wall induced dipole field (large red arrows). a) Splay wall, b) Néel wall.

across the wall, as shown in Figs. 12-13. In these figures, the field profile *per* atomic layer is plotted *vs* distance from the wall center. Profiles are shown only for the upper half of the layer thickness and symmetry *vs* the layer mid-plane provides the missing profiles. Figs. 12 and 13 show that the z field component is wall-type specific and globally independent of the lattice. The residual field proves rather small with amplitude in the $10-20$ mT range for Splay walls, ≈ 4 times smaller for Néel walls and only weakly dependent on the atomic layer index.

In each F-ordered atomic layer parallel to the surface, a Splay wall gives rise to so-called σ charges, a Néel wall to dipolar or π charges as schematically shown in Fig. 14. Charges change sign with each unit increase or decrease of the layer index. In order to deal with fully compensated AF epilayers, we have solely considered an even number of atomic layers, be it for a *bcc* or a *fcc* lattice. Then, for any atomic layer in Fig.14, pair summation, starting with the two layers adjacent to that under consideration, does not lead to a full balance of the fields. Thusly, a monopolar z component field is expected for a Splay wall, dipolar for a Néel wall, the sign of which is defined by the sign of charges closest to the interface and the free surface. It has been checked that the z field component reverses with a global reversal of the spin orientation.

According to the $(\mathbf{l}, \mathbf{m})$ decomposition scheme, the exact opposite result would have been reached. Although at first puzzling, this result is easily understood after realizing that, since $\mathbf{l} \perp \mathbf{m}$, the corresponding $\mathbf{m}$ wall is, for a Splay wall, akin a Néel wall and *vice versa* (see e.g. Fig.7 in [36]). As such, however, the pure 'at lattice points' point dipole theory is not free of critics, either, as noticed early in [60] when alluding to weak disorder. The very fact that the 'at lattice points' picture proves sensitive to the exact local dipoles positions means a restriction to low temperatures.

Practically, dipole fields evaluation highly benefits from Fast Fourier Transforms (FFT) techniques as soon as the dipole distribution may be dispatched into as necessary a number of ferromagnetic tetragonal sublattices. The *bcc* case is simple, with only two sublattices. The *fcc*

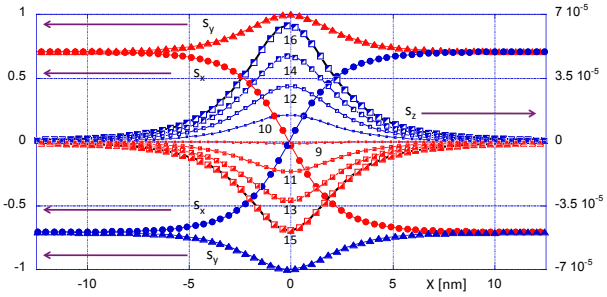

FIG. 15. Splay wall profile in a *bcc* lattice after relaxation including anisotropy, exchange and dipole-dipole interactions. Left scale: s_x and s_y spin components in the two top atomic layers, index 15 (red symbols) and 16 (blue symbols); right scale: s_z spin component in the 8 topmost atomic layers indexed $16, 15, ..., 9$, the missing profiles being obtained by symmetry around the epilayer mid-plane.

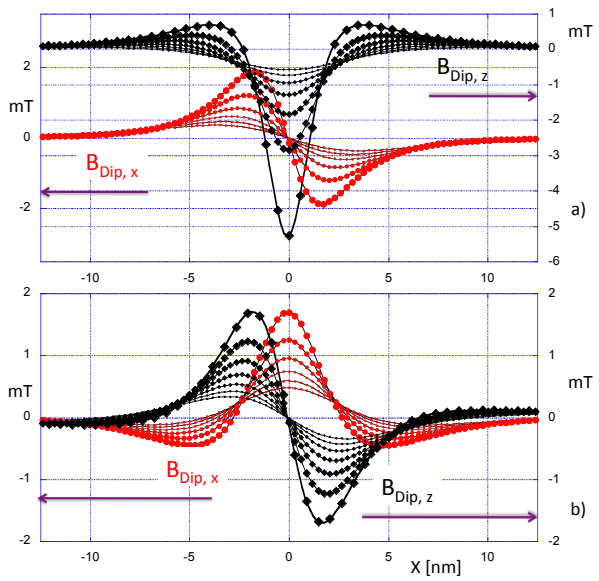

FIG. 16. Dipole field distribution above the free surface for a) a Splay wall in a *bcc* lattice, b) a Néel wall in a *fcc* lattice. Left scale: B_x (mT); right scale: B_z (mT). B_x profiles at distances a) 1, 2 .., 6 nm, b) 0.5, 1, .., 3 nm from the free surface; B_z profiles at surface level and distances a) 1, 2 .., 6 nm, b) 0.5, 1, .., 3 nm from the free surface.

case proves much more demanding due to the incompatibility between an ABC sequence of (111) planes and the bi-(111) planes AF ordering, meaning a 6 (111) planes sequence, as recalled in Fig.11. This added complexity may, however, rather easily be mastered. In this work, FFT techniques have been implemented overall and care has been taken to make sure that the FFT dipole fields evaluations were exactly equivalent to direct sum estimates. It remains nevertheless true that dipole fields estimates remain sensitive to the boundary conditions imposed by a finite size 'computation box'. In the computation axes of Figs.3 or 6, the y and z computation box limits are physically linked to the AF stripe width and epilayer thickness, respectively. The x limits are computation specific and care needs to be experienced in order to make sure that the x limits have the minimal incidence on the final results.

Altogether, dipole fields exert a rather tiny influence on the converged wall textures, up to the point, actually, where it proves difficult to display their influence at the graph level, except for the s_z spin component that remains smaller than 10^{-4} under the prevailing anisotropy as displayed in Fig.15 (the noise level in these computations is of the order of 10^{-15}). Similar results are obtained for Splay walls within a *fcc* lattice whereas Néel walls display bimodal s_z profiles for both lattice types.

On the other hand, dipole fields allow for an estimate of the fringing field below the interface or above the free surface of the AF epilayer that may cast new insights into AF wall observability by means of, for instance, NV microscopy (e.g. [65] and *loc.cit.*). Fig.16 displays the x and z components of the fringing field above the free surface corresponding to a) a Splay wall in a *bcc* lattice and b) a Néel wall in a *fcc* lattice. In the Splay wall case, the z component of the fringing field outside and wall-induced dipole field inside (Fig.12) are both primarily unimodal, changing sign, however, upon crossing the free surface, in relation with the wall charge distribution just below the free surface (Fig.14). Similar arguments hold true for the Néel wall. Such features, characteristic of ferromagnets, therefore find their counterpart in AF's, at least in layered AF's, such as those considered here. As anticipated, the fringing field decays rapidly with distance from the surface: the Splay wall z field component drops to less than 0.15 mT at 15 nm from the surface and its Néel wall counterpart to roughly the same value at only 5 nm.

A last remark ought to be made at the end of this section if wishing to find which part of the dipolar energy ought to be attributed to a wall. The only suggestion, here, is to perform the difference between the dipolar energies linked to two identical volumes, one containing a fully relaxed wall, the second solely containing the two domains separated by an abrupt transition. Following this procedure for instance for the Splay wall in a *bcc* lattice, one finds $\Delta E_{\rm Dip} = -92.02 - (-94.94) = 2.9$ meV, *i.e.* a value small w.r.t. the exchange or anisotropy energies within the same volume (Section III A).

V. LATTICE INFLATION AS A ROUTE TOWARDS AF MICROMAGNETICS

Although the exchange energy per link is clearly associated to a precise distance between n.n. or n.n.n., no length explicitly enters the expressions of the exchange or anisotropy effective fields. It follows that lattice inflation, or swelling, allows for the computation of AF textures in larger volumes whilst preserving the native ordering within a given lattice. Defining the swelling ratio as S_w, a pure number, the material parameters need

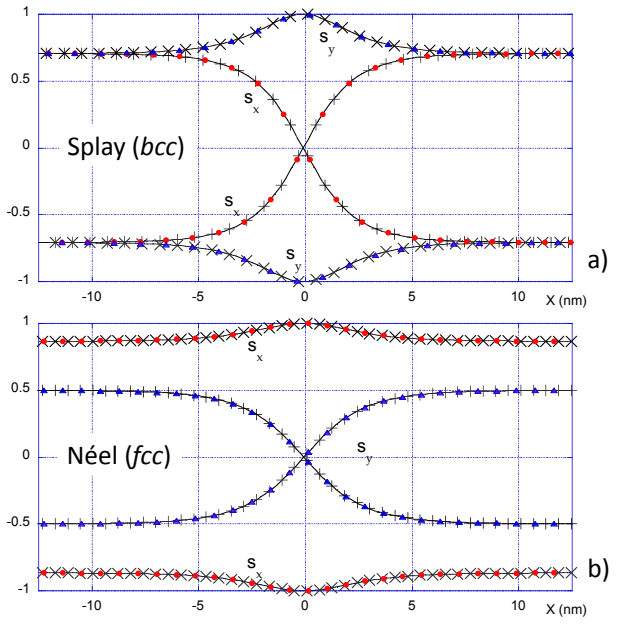

FIG. 17. Splay (*bcc*) and Néel (*fcc*) wall profiles as a function of lattice swelling ratio S_w. Continuous lines: native lattice, + and × symbols: $S_w = 2$, full red and blue symbols: $S_w = 3$.

to be scaled as $a \Rightarrow S_w a$, $J_{ij} \Rightarrow S_w J_{ij}$, $d_{\rm DMI} \Rightarrow S_w d_{\rm DMI}$ and $\mu_s \Rightarrow S_w^3 \mu_s$, $k \Rightarrow S_w^3 k$ in order to keep their continuum limit equivalents constant. We stress that characteristic lengths such as the wall width are left untouched in the swelling process. The wall energy per unit area is equally conserved. No rescaling of time needs to be envisaged, leaving an open access to the full physical frequency range, in particular those large frequencies imposed by the exchange field. Inversely, the swelling process introduces a cut-off in the spin-wave (or phonon) spectrum. Such properties evoke micromagnetics in ferromagnets, with, however, one difference: in F's, the continuum limit is commonly viewed as an intermediary step between atomistic modeling and projection onto a suitable mesh, the size of which is conditioned by the characteristic lengths of the system. Here, lattice-compliant inflation allows the intermediary step to be skipped. Swelling ratios in the range $2-5$ may easily be used, thereby potentially reducing the number of lattice points by a factor S_w^3 for a given physical volume.

Validation of the lattice-compliant inflation scheme in the static limit may be gained from the inspection of Fig.17 comparing wall profiles for two values of the swelling ratio, in both lattices. Only a slight global translation of the profiles w.r.t. the native lattice profile has been allowed for in order to keep a common wall centre. The agreement between profiles proves excellent.

Unfortunately, the inclusion of dipole-dipole interactions is more problematic due to the alternate nature of the dipole fields sums in AF's and their truncation in ultra-thin layers. Reducing the dipolar energy to a local anisotropy energy certainly helps, at least when almost constant across the thickness as such is the case for the *fcc* lattice. Reducing dipolar energy to anisotropy implies, however, the neglect of wall specific dipolar interactions. Those have been shown above to be small, but nevertheless real.

VI. ACTION OF SPIN-ORBIT TORQUES

Recently investigated metallic AF compounds include CuMnAs, Mn_2Au, and IrMn or PtMn [9–16]. The collinear antiferromagnets CuMnAs and Mn_2Au have in common a tetragonal unit cell and a "staggered" stacking of (001) planes meaning alternate spin orientations in successive (001) planes. Insulating AF compounds include CoO and NiO and the weak ferromagnet Fe_2O_3 [17–21]. Depending, however, on the substrate orientation, these collinear antiferromagnets may exhibit different preferred orientations of the order parameter. For instance, if grown on Pt(111) or MgO(111), NiO exhibits preferred spin orientations in the (111) plane [17]. If grown on MgO(001), the preferred orientations in strained CoO or NiO epilayers belong anew to the growth plane, and follow $\langle 110 \rangle$ directions [18–20, 49]. Note that, in neither case, is the spin ordering precisely known. If the general picture pertaining to bulk NiO or CoO holds true, *i.e.* alternate spin orientations in successive {111} planes, then the [110] and $[1\bar{1}0]$ directions are, in any given (001) plane, inequivalent in terms of spin stacking as demonstrated experimentally at the free surface of a NiO crystal [66].

Conducting and insulating AF's also differ in the nature of the current induced spin-torque. In the metallic structures CuMnAs, Mn_2Au, the charge current is meant to flow homogeneously through the AF layer. For the insulating compounds, the current flows within an adjacent heavy metal layer, Pt most often. In one scenario, the spin polarization of carriers flowing across the heavy metal layer splits in the presence of spin-orbit interactions (Spin Hall Effect) and the associated spin-current may be absorbed at the interface [67, 68]. A charge current flowing parallel to an interface with naturally broken inversion symmetry may also, in the presence of spin-orbit interactions, generate spin currents [69]. Spin-orbit interactions imply a correlation between the conduction electrons momentum and their spin. Such concepts extended to conducting antiferromagnets with adequate structural characteristics lead to a spin-polarization unbalance *per* sub-lattice, with, as a consequence, a modulation of the carriers spin-polarization at the atomic scale [9, 70].

From a purely geometrical point of view, however, torques acting on the localized moments may be simply differentiated as *field-like*, $\tau_{\rm FL} \propto \hat{\mathbf{s}} \times \hat{\mathbf{p}}$, and *damping-like*, $\tau_{\rm DL} \propto \hat{\mathbf{s}} \times (\hat{\mathbf{s}} \times \hat{\mathbf{p}})$, where $\hat{\mathbf{s}}$ and $\hat{\mathbf{p}}$ are unit vectors along the localized moment and the polarization of the local spin current, respectively [69]. Application to antiferromagnets swiftly reveals the kind of interchange occurring

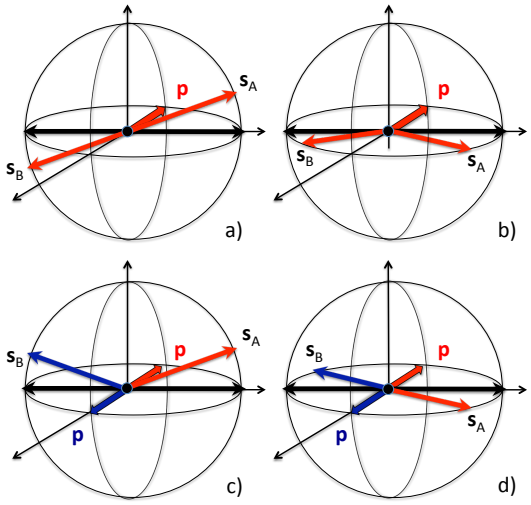

FIG. 18. Action of the field-like (a,c) and damping-like (b,d) spin-orbit torques on an AF coupled bi-spin ($\mathbf{S}_A, \mathbf{S}_B$) in the case of a,b) a uniform polarization $\mathbf{p}$ of the spin current, c,d) a staggered polarization. Black arrows: initial spin orientation; red or blue arrows: spin orientation upon application of the torque.

between the field-like and damping-like torques whether $\hat{\mathbf{p}}$ is uniform or reverses with $\hat{\mathbf{s}}$, see Fig. 18.

The first experiments [9, 17] attempted to demonstrate a direct electrical control of the AF order parameter by spin-orbit torques (SOT). Shortly after, however, the observation of domains in CuMnAs proved that wall motion indeed offers an alternative mechanism [11]. Similarly, in NiO, spin-orbit torques resulting from the application of current pulses were shown to lead to important reorganisations of the domain pattern [71]. On the other hand, current pulses in these early experiments prove altogether alarmingly long compared to typical precession times in AF's.

We consider first below the action of SOT's on the spin orientation within small volumes with uniform order parameter, second, the action of SOT's on certain wall types in the presence of DM interactions, still within the lattice-compliant formulation of the present work. More precisely, we now consider epitaxial AF layers with a *bcc* or *fcc* lattice in contact with a heavy metal layer. We assume the current to flow solely in the heavy metal layer: in the axes of Figs.3 or 6, a charge current flowing along the x direction produces a spin current polarized along the y direction. We do not envisage here the more complex case of systems like CuMnAs with their staggered spin-orbit fields (see [72]).

Fields corresponding to the SOT's may now be added to the effective field, namely $\mathbf{B}_{\rm DL} = B_{\rm D}\,[\hat{\mathbf{s}} \times \hat{\mathbf{y}}]$; $\mathbf{B}_{\rm FL} = B_{\rm F}\hat{\mathbf{y}}$; $B_{\rm D} = \frac{\hbar}{2}\frac{J}{e}\frac{\mathcal{A}}{\mu_s}\Phi_{\rm SH}$; $B_{\rm F} = \chi B_{\rm D}$ where, $B_{\rm D}$ and $B_{\rm F}$ are the moduli of the damping-like and field-like Spin Hall fields and χ the ratio between them, J is the current density in the heavy metal layer and $\mathcal{A}$ the area per spin in the interface plane, e the electron charge ($e < 0$) and $\Phi_{\rm SH}$ the Spin Hall angle. For the *bcc* lattice, $\mathcal{A}$ is equal to a^2 for a (001) interface, $d_{nn}^2\sqrt{3}/2$ for the (111) interface of a *fcc* lattice. The above definition implies the SOT to be applied into a single atomic layer within the AF, namely that located at the interface. In the following, we stick to that definition, exchange interactions relaying the torque in the upper AF layers. Distributing the torque would have been equally possible. The difference between the two approaches actually remains immaterial.

Finally, DM interactions have been experimentally shown to lead to remarkable spin textures in ultra-thin films such as spin spirals, homochiral successive walls or a skyrmion lattice [73–75]. The present implementation into an atomistic code adopts the 3 ions mechanism of Levy and Fert [76], owing to which two spin carrying ions belong to the interface plane, one ion, non-magnetic, to the layer just below/above. We also consider at first a fully crystalline stack, so that the non-magnetic ion remains in an epitaxial relation with the spin carrying layer. Practically, for a (001) interface within a *bcc* lattice, the spin carrying ions are n.n.n.'s and the non magnetic ion a n.n.. For each link in the interface plane, there exist two n.n. non magnetic ions in the heavy metal, justifying the use of the expression $\mathbf{D}_{ij} = d_{\rm DMI}(\hat{\mathbf{u}}_{ij} \times \hat{\mathbf{z}})$ in the DM interactions energy. For a (111) interface within a *fcc* lattice, neighbours in the interface plane are n.n.'s whilst n.n.n.'s control exchange interactions within the AF layer. More importantly, for each link in the interface plane, there exists a single n.n. non magnetic ion [77] so that $\mathbf{D}_{ij}$ does not any more belong to the interface plane. Moreover, two successive links around a given spin at the interface share a common n.n. non-magnetic ion. It follows that the out of plane component of the Dzyaloshinskii vector alternates at the atomic scale in full similarity to the Co/Pt(111) case. Although calling for further insight, we prefer at this stage to keep a unique definition of the Dzyaloshinskii vector. Then, for both lattices, the two magnetic ions belong to the interface and so does $\mathbf{D}_{ij}$. It ensues that a gain in DM interactions energy may only be achieved if the spin orientation leaves the interface plane.

All calculations below have been performed for purely indicative parameters, namely $|d_{\rm DMI}| = 1.5$ meV, $J = -50$ GA/m^2, $\Phi_{\rm SH} = 0.1$, $\chi = 0$ or 0.25 and damping parameter $\alpha = 0.01$.

A. Uniform order parameter

The main result in this section is that, switching-on the current only leads, whether $\chi = 0$ or 0.25, to a minute reorientation of the spins, in full similarity with the ferromagnetic case. This minute reorientation occurs within a few ps for damping parameters in the 10^{-2} range. For experimentally accessible currents, a direct control of the AF order parameter [78] proves simply out of reach, except, perhaps, for situations where huge spin currents result from the fast demagnetization of an adjacent fer-

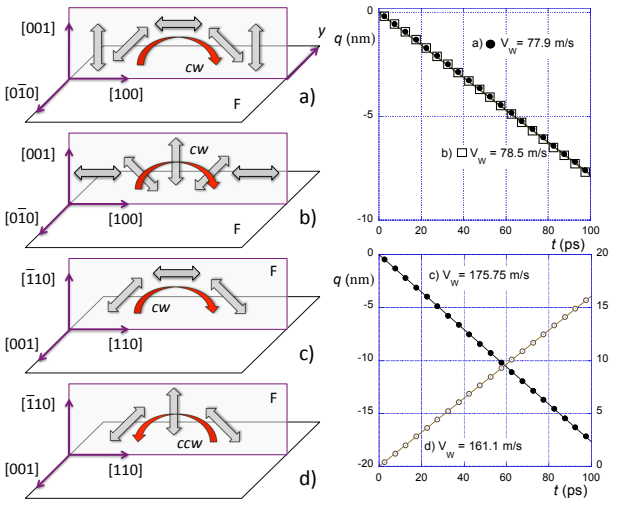

FIG. 19. Spin textures and velocity under SOT. Left: four different spin textures within a *bcc* lattice with $\hat{\mathbf{y}}$ chirality axis. a,b) (001) interface, (010) easy plane and a) [001], b) [100] easy axis; c,d) ($\bar{1}$10) interface, ⟨100⟩ easy axes within the (001) plane. Right: wall velocity under spin-orbit torques. Simulation parameters: $J = -50$ GA/m^2, $\Phi_{\rm SH} = 0.1$, $\chi = 0$ and $\alpha = 0.01$. $d_{\rm DMI} = +1.5$ meV(a, b, d), -1.5 meV(c).

romagnetic layer [26].

Obviously, a drastically different scenario develops if, instead of starting with a spin orientation at equilibrium, one starts with a metastable equilibrium state. Such would be the case should the anisotropy landscape be altered due to e.g. rising thermal strains [79]. Sadly so, however, the SOT becomes simply superfluous.

B. Spin textures

Néel type walls within a ferromagnet (F) with perpendicular anisotropy have been shown to move with speeds up to a few 100 m/s under the action of SOT's in the presence of DM interactions [80]. More recently, walls within F stripes with an in-plane magnetization were also shown to move, albeit with a lesser velocity, due to cycloidal distortions of the domain wall structure associated with DM interactions [81]. In their 1D study of simple walls in AF's, Shiino *et al.* do find that (x, z) plane Néel and Splay walls (resp. z and x axis uniaxial anisotropy) propagate with similar velocities under SOT's in the presence of DM interactions ([31] and associated Supplemental Material).

The results of the present study are similar. In a nutshell, fully planar ((x, y) plane) spin textures, whether Néel or Splay do not propagate under SOT's, both in the *bcc* or *fcc* lattice, even in the presence of DM interactions. These results are in line with a previous remark stating that DM interactions may only have a bearing when the out-of-plane spin component ceases to be zero and dipole field interactions are simply too weak to provide the necessary action. On the other hand, wall structures in AF's potentially leading to a high mobility under SOT's may be thought of.

In the *bcc* lattice, such walls include, for a (001) interface and a (010) easy plane, a 180° Néel (Splay) wall in a system with leading perpendicular ([100] axis uniaxial) anisotropy, and for a (110) interface, a 90° Néel or Splay wall. For the whole set of spin textures, (001) remains the ferromagnetic plane. The first two and last two structures are characterized by fully uncompensated (the 1st layer is ferromagnetic) and fully compensated interfaces, respectively. More precisely, each ↑ spin belonging to the ($\bar{1}$10) *bcc* interface has four ↓ n.n.n.'s, and *vice versa*. All these walls are chiral with a chirality axis along $\hat{\mathbf{y}}$ and, thus, couple efficiently to the damping-like SO field. Note that the wall chirality proves common to the various F sub-lattices. Results are summarized in Fig.19. For these simulations, an initial clockwise (cw) chirality has been imposed to the spin textures (a)-(c), anticlockwise (ccw) for (d). Then, the correct sign is assigned to the DM interactions parameter $d_{\rm DMI}$ so as to lead to a gain in DM energy. Physically, this would mean a particular choice for the heavy metal in contact with the AF layer. The inspection of Fig.19 indicates that, for a cw chirality, $d_{\rm DMI}$ needs to be > 0 in the case of a ferromagnetic interface, < 0 for a fully compensated AF interface, as a direct consequence of the vector product entering the expression of the DM energy. The sign of $d_{\rm DMI}$ also needs to reverse with chirality. Owing to conventions valid here, a negative current density pushes a cw texture towards $x < 0$, a ccw texture towards $x > 0$. The analogy between ferromagnets [80] and antiferromagnets is thus, here also, striking.

Current densities in this work are in the low end of the density spectrum addressed in [31]. Furthermore, a rather conservative value of the damping parameter has been chosen ($\alpha = 10^{-2}$). Wall velocities in the present lattice-compliant approach of AF's prove therefore equivalent to velocities reached in [31], *i.e.* velocities in the km/s range for $\alpha = 10^{-3}$. Pending a detailed analysis, the velocity scatter in Fig.19 is to be attributed mostly to the variation in wall width, itself a function of the anisotropy landscape.

Lastly, we consider, for the *fcc* lattice, two spin textures, a Néel and a Splay wall, schematically represented in Fig.20 and equivalent to the textures in Fig.19 c-d. These still are spin textures belonging to a single (111) AF2 ordered Twin domain but now with a (1$\bar{1}$0) interface. Similarly to the *bcc* case, the interface is compensated with also each ↑ spin belonging to the interface having four ↓ neighbours, and *vice versa*. The exact geometry proves, however, different since two of the ↓ spins are n.n.'s, two n.n.n.'s. Although possibly calling for the definition of two DMI parameters, we treat them here indifferently. Both of these walls are found to propagate effortless under damping-like SOT's provided n.n. exchange interactions are turned off [82]. As above, variations in velocity, here minute, are ascribable

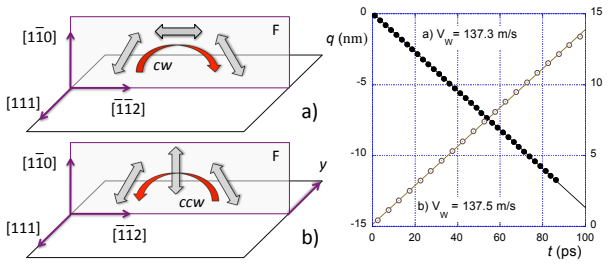

FIG. 20. Spin textures and velocity under SOT. Left: two different spin textures within a *fcc* lattice with $\hat{\mathbf{y}}$ chirality axis, $(1\bar{1}0)$ interface and $\langle\bar{2}11\rangle$ easy axes within the (111) plane. Right: wall velocity under spin-orbit torques. Simulation parameters: $J_1 = 0$, $J = -50$ GA/m^2, $\Phi_{\rm SH} = 0.1$, $\chi = 0$ and $\alpha = 0.01$. $d_{\rm DMI} = -1.5$ meV$(a), +1.5$ meV(b).

to anisotropy induced wall width modulations.

Summarizing, domain wall mobility under SOT's in antiferromagnets is clearly related to wall geometrical characteristics, in full analogy with ferromagnets. It is therefore not surprising that wall mobility under SOT be largely independent of the subtending lattice. Similarly to the F case, successive partial angle walls in AF's (90° in *bcc* or, 60° or 120° in *fcc* structures) may not be homochiral, and thus, may only move towards or away from each other under SOT's.

VII. OUTLOOK

In the absence of DM interactions, wall textures in ferromagnets are often the result of competing interactions between anisotropy characteristics and sample specific demagnetizing field distributions, exchange interactions being mostly isotropic. In AF's, anisotropy and lattice-compliant exchange interactions set the rules. In particular, magnetostrictive spontaneous deformations and, at a first level, strain-induced anisotropy play a particular role. The latter have been neglected in this work as, except for the most recent work [79], in many previous studies and a suitable continuum mechanics remedy beyond strain-induced anisotropy needs to be found. On the other hand, this work casts new insights into the role of lattice-compliant exchange interactions and 'at lattice points' dipole fields. Lattice-compliant Heisenberg exchange interactions are the only needed exchange interactions in the bulk of AF's with inversion symmetry. Owing to lattice and wall geometry, these may, or not, induce phase lags in the spin canting between sub-lattices. Although complex, 'at lattice points' dipole-dipole interactions respect basic symmetries. Neither of these characteristics is met in the $(\mathbf{l}, \mathbf{m})$ decomposition models developed recently. Both for exchange and dipoles interactions, the lattice-compliant and the $(\mathbf{l}, \mathbf{m})$ decomposition model differ basically in the location assignment of two neighbouring AF coupled spins and the difference appears irreducible. An alternative, lattice-compliant, route towards AF micromagnetics is also being proposed. A finely tuned comparison with multipole-inspired models [83] probably proves at this stage desirable.

ACKNOWLEDGMENTS

This work was supported by the French Agence Nationale de la Recherche (project PIAF, ANR-17-CE09-0030). Enriching discussions with A. Mougin, M. Viret, F. Piéchon and P. Simon, as well as a genuinely critical reading of the manuscript by S. Rohart are gratefully acknowledged.

[1] C. Kittel, Phys. Rev. **82**, 565 (1951).
[2] F. Keffer and C. Kittel, Phys. Rev. **85**, 329 (1952).
[3] M. Hagiwara, K. Katsumata, H. Yamaguchi, M. Tokunaga, I. Yamada, M. Gross, and P. Goy, International Journal of Infrared and Millimeter Waves **20**, 617 (1999).
[4] M. Hagiwara and K. Katsumata, Riken Review **24**, 13 (1999).
[5] F. Keffer and W. O'Sullivan, Phys. Rev. **108**, 637 (1957).
[6] J. Milano, L. B. Steren, and M. Grimsditch, Phys. Rev. Lett. **93**, 077601 (2004).
[7] D. MacNeill, J. T. Hou, D. R. Klein, P. Zhang, P. Jarillo-Herrero, and L. Liu, Phys. Rev. Lett. **123**, 047204 (2019).
[8] V. G. Bar'yaktar, M. V. Chetkin, B. A. Ivanov, and S. N. Gadetskii, *Dynamics of Topological Solitons, Experiments and Theory*, Springer Tracts in Modern Physics (Springer, 1994).
[9] P. Wadley, B. Howells, J. Železný, C. Andrews, V. Hills, R. P. Campion, V. Novák, F. Freimuth, Y. Mokrousov, A. W. Rushford, K. W. Edmonds, B. W. Gallagher, and T. Jungwirth, Science **351**, 587 (2016).
[10] M. J. Grzybowski, P. Wadley, K. W. Edmonds, R. Beardsley, V. Hills, R. P. Campion, B. W. Gallagher, J. S. Chauhan, V. Novak, T. Jungwirth, F. Maccherozzi, and S. S. Dhesi, Phys. Rev. Lett. **118**, 057501 (2017).
[11] P. Wadley, S. Reimers, M. J. Grzybowski, C. Andrews, M. Wang, J. S. Chauhan, B. L. Gallagher, R. P. Campion, K. W. Edmonds, S. S. Dhesi, F. Maccherozzi, V. Novak, J. Wunderlich, and T. Jungwirth, Nat. Nanotechnol. **13**, 362 (2018).
[12] S. Bodnar, L. Šmejkal, I. Turek, T. Jungwirth, O. Gomonay, J. Sinova, A. Sapozhnik, H.-J. Elmers, M. Kläui, and M. Jourdan, Nat. Commun. **9**, 348 (2018).
[13] X. F. Zhou, J. Zhang, F. Li, X. Z. Chen, G. Y. Shi, Y. Z. Tan, Y. D. Gu, M. S. Saleem, H. Q. Wu, F. Pan, and C. Song, Phys. Rev. Applied **9**, 054028 (2018).
[14] M. Meinert, D. Graulich, and T. Matalla-Wagner, Phys. Rev. Applied **9**, 064040 (2018).
[15] H. Reichlová, D. Kriegner, V. Holý, K. Olejník, V. Novák, M. Yamada, K. Miura, S. Ogawa, H. Taka-

hashi, T. Jungwirth, and J. Wunderlich, Phys. Rev. B **92**, 165424 (2015).
[16] S. DuttaGupta, A. Kurekov, O. A. Tetriakov, G. Krishnaswamy, G. Sala, V. Krizakova, F. Maccherozzi, D. S. Dhesi, P. Gambardella, S. Fukami, and H. Ohno, Nat. Commun. **11**, 5715 (2018).
[17] T. Moriyama, K. Oda, T. Ohkochi, M. Kimata, and T. Ono, Scientific Reports **8**, 14167 (2018).
[18] X. Z. Chen, R. Zarzuela, J. Zhang, C. Song, X. F. Zhou, G. Y. Chi, F. Li, H. A. Zhou, W. J. Jiang, F. Pan, and Y. Tserkovnyak, Phys. Rev. Lett. **120**, 207204 (2018).
[19] L. Baldrati, C. Schmitt, O. Gomonay, R. Lebrun, R. Ramos, E. Saitoh, J. Sinova, and M. Kläui, Phys. Rev. Lett. **125**, 077201 (2020).
[20] F. Schreiber, L. Baldrati, C. Schmitt, , R. Ramos, E. Saitoh, R. Lebrun, J. Sinova, and M. Kläui, Appl. Phys. Lett. **117**, 082401 (2020).
[21] P. Zhang, J. Finley, T. Safi, and L. Liu, Phys. Rev. Lett. **123**, 247206 (2019).
[22] T. Jungwirth, X. Marti, P. Wadley, and J. Wunderlich, Nat. Nanotechnol. **11**, 231 (2016).
[23] B. Skubic, J. Hellsvik, L. Nordström, and O. Eriksson, J. Phys.: Condens. Matter **20**, 315203 (2008).
[24] R. F. L. Evans, W. J. Fan, P. Chureemart, T. A. Ostler, M. O. A. Ellis, and R. W. Chantrell, J. Phys.: Condens. Matter **26**, 103202 (2014).
[25] G. P. Müller, M. Hoffmann, C. Dißelkamp, D. Schürhoff, S. Mavros, M. Sallerman, N. S. Kiselev, H. Jónsson, and S. Blügel, Phys. Rev. B. **99**, 224414 (2019).
[26] T. Chirac, J.-Y. Chauleau, P. Thibaudeau, O. Gomonay, and M. Viret, Phys. Rev. B. **102**, 134415 (2020).
[27] S. Selzer, U. Atxitia, U. Ritzmann, D. Hinzke, and U. Nowak, Phys. Rev. Lett. **117**, 107201 (2016).
[28] R. M. Otxoa, U. Atxitia, P. E. Roy, and O. Chubykalo-Fesenko, Communications Physics **3**, 31 (2020).
[29] D. R. Rodrigues, A. Salimath, K. Everschor-Sitte, and K. M. D. Hals, Phys. Rev. Lett. **127**, 157203 (2021).
[30] N. Papanicolaou, Phys. Rev. B. **51**, 15062 (1995).
[31] T. Shiino, S.-H. Oh, P. M. Haney, S.-W. Lee, G. Go, B.-G. Park, and K.-J. Lee, Phys. Rev. Lett. **117**, 087203 (2016).
[32] T. Conzelmann, S. Selzer, and U. Nowak, J. Appl. Phys. **127**, 223908 (2020).
[33] V. G. Bar'yaktar and B. A. Ivanov, Solid State Communications **34**, 545 (1980).
[34] A. F. Andreev and V. I. Marchenko, Sov. Phys. Usp. **23**, 21 (1980).
[35] F. D. M. Haldane, Phys. Rev. Lett. **50**, 1153 (1983).
[36] E. G. Tveten, T. Müller, J. Linder, and A. Brataas, Phys. Rev. B. **93**, 104408 (2016).
[37] A. Manchon, J. Železný, I. M. Miron, T. Jungwirth, J. Sinova, A. Thiaville, K. Garello, and P. Gambardella, Rev. Mod. Phys. **91**, 035004 (2019).
[38] K. Momma and F. Izumi, J. Appl. Crystallogr. **44**, 1272 (2011).
[39] M. N. Baibich, J. M. Broto, A. Fert, F. Nguyen Van Dau, F. Petroff, P. Etienne, G. Creuzet, A. Friederich, and J. Chazelas, Phys. Rev. Lett. **61**, 2472 (1988).
[40] G. Binasch, P. Grünberg, F. Saurenbach, and W. Zinn, Phys. Rev. B. **39**, 4828 (1989).
[41] S. Blügel, M. Weinert, and P. H. Dederichs, Phys. Rev. Lett. **60**, 1077 (1988).
[42] S. Blügel, D. Pescia, and P. H. Dederichs, Phys. Rev. B. **39**, 1392 (1989).
[43] H. Zabel, J. Phys.: Condens. Matter **11**, 9303 (1999).
[44] P. J. Berlowitz and N. D. Shinn, Surface Science **209**, 345 (1989).
[45] P. Bödeker, A. Hucht, A. Schreyer, J. Borchers, F. Güthoff, and H. Zabel, Phys. Rev. Lett. **81**, 914 (1998).
[46] H. Bizette, C. F. Squire, and B. Tsai, C. R. Acad. Sci. **207**, 449 (1938).
[47] S. D. Peacor and T. Hibma, Surface Science **301**, 11 (1994).
[48] A. Rota, S. Altieri, and S. Valeri, Phys. Rev. B. **79**, 161401(R) (2009).
[49] J. Zhu, Q. Li, J. X. Li, Z. Ding, J. H. Liang, X. Xiao, Y. M. Luo, C. Y. Hua, H.-J. Lin, T. W. Pi, Z. Hu, C. Won, and Y. Z. Wu, Phys. Rev. B **90**, 054403 (2014).
[50] S. I. Csiszar, M. W. Haverkort, Z. Hu, A. Tanaka, H. H. Hsieh, H. J. Lin, C. T. Chen, T. Hibma, and L. H. Tjeng, Phys. Rev. Lett. **95**, 187205 (2005).
[51] F. Cinquini, L. Giordano, G. Pacchioni, A.-M. Ferrari, C. Pisani, and C. Roetti, Phys. Rev. B. **74**, 165403 (2006).
[52] G. Fisher, M. Däne, A. Ernst, P. Bruno, M. Lüders, Z. Szotek, and W. Temmerman, Phys. Rev. B. **80**, 014408 (2009).
[53] P. García-Fernández, J. C. Wojdeł, J. Íñiguez, and J. Junquera, Phys. Rev. B. **93**, 195137 (2016).
[54] M. T. Hutchings and E. J. Samuelsen, Phys. Rev. B. **6**, 3447 (1972).
[55] M. Kléman, *Points, Lines and Walls* (Wiley, Chichester, 1983).
[56] Initial spin distribution: uniform (↑,↓) spin distribution along the local easy axis within domains, uniform (↑,↓) spin distribution within wall width (schematic) and exalted, hence pinning, anisotropy along the computation box lateral edges normal to x.
[57] W. L. Roth, J. Appl. Phys. **31**, 2000 (1960).
[58] G. A. Slack, J. Appl. Phys. **31**, 1571 (1960).
[59] Anisotropy values may appear large if compared to the sole cubic anisotropy [64], less so if incorporating magnetoelasticity at 1st order and dipole-dipole interactions [6]. Moreover, variations in anisotropy parameters may solely affect quantitatively the present results, not qualitatively.
[60] J. M. Luttinger and L. Tisza, Phys. Rev. **70**, 954 (1946).
[61] J. M. Luttinger and L. Tisza, Phys. Rev. **72**, 257 (1947).
[62] J. A. Sauer, Phys. Rev. **57**, 142 (1940).
[63] T. Yamada, J. Phys. Soc. Jpn **21**, 650 (1966).
[64] T. Yamada, J. Phys. Soc. Jpn **21**, 664 (1966).
[65] M. S. Wörnle, P. Welter, M. Giraldo, T. Lottenmoser, M. Fiebig, P. Gambardella, and C. L. Degen, Phys. Rev. B. **103**, 094426 (2021).
[66] U. Kaiser, A. Schwarz, and R. Wiesendanger, Nature **446**, 522 (2007).
[67] K. Ando, S. Takahashi, K. Harii, K. Sasage, J. Ieda, D. Maekawa, and E. Saitoh, Phys. Rev. Lett. **101**, 036601 (2008).
[68] L. Liu, T. Moriyama, D. C. Ralph, and R. A. Buhrmann, Phys. Rev. Lett. **106**, 036601 (2011).
[69] V. P. Amin, J. Zemen, and M. D. Stiles, Phys. Rev. Lett. **121**, 136805 (2018).
[70] J. Železný, H. Gao, K. Výborný, J. Zemen, J. Mašek, A. Manchon, J. Wunderlich, J. Sinova, and T. Jungwirth, Phys. Rev. Lett. **113**, 157201 (2014).

[71] M. Wörnle, P. Welter, Z. Kašpar, K. Olejník, V. Novák, R. Campion, P. Wadley, T. Jungwirth, C. Degen, and P. Gambardella, arXiv:1912.05287.
[72] O. Gomonay, T. Jungwirth, and J. Sinova, Phys. Rev. Lett. **117**, 017202 (2016).
[73] M. Bode, M. Heide, K. von Bergmann, P. Ferriani, S. Heinze, G. Bihlmayer, A. Kubetzka, O. Pietzsch, S. Blügel, and R. Wiesendanger, Nature **447**, 190 (2007).
[74] P. Ferriani, K. von Bergmann, E. Vedmedenko, S. Heinze, M. Bode, M. Heide, G. Bihlmayer, S. Blügel, and R. Wiesendanger, Phys. Rev. Lett. **101**, 027201 (2008).
[75] S. Heinze, K. von Bergmann, M. Menzel, J. Brede, A. Kubetzka, R. Wiesendanger, G. Bihlmayer, and S. Blügel, Nat. Phys. **7**, 713 (2011).
[76] P. M. Levy and A. Fert, Phys. Rev. B **23**, 4667 (1981).
[77] A. Crépieux and C. Lacroix, J. Magn. Magn. Mat. **182**, 341 (1998).
[78] H. V. Gomonay and V. M. Loktev, Phys. Rev. B. **81**, 144427 (2010).
[79] H. Meer, F. Schreiber, C. Schmitt, R. Ramos, E. Saitoh, O. Gomonay, J. Sinova, L. Baldrati, and M. Kläui, arXiv:2008.05219.
[80] A. Thiaville, S. Rohart, É. Jué, V. Cros, and A. Fert, EPL (EuroPhysics Letters) **100**, 57002 (2012).
[81] R. Kohno, J. Sampaio, S. Rohart, and A. Thiaville, Phys. Rev. B **102**, 020410(R) (2020).
[82] The competition between DM and Heisenberg exchange interactions inducing non-collinear and collinear spin structures, respectively, may lead to complex magnetic ground states (see e.g. [84]). Frustration may clearly add to the overall complexity and, at this stage, has been left out for further insight.
[83] M.-T. Suzuki, T. Koretsune, M. Ochi, and R. Arita, Phys. Rev. B **95**, 094406 (2017).
[84] N. Romming, H. Pralow, A. Kubetzka, M. Hoffmann, S. von Malottki, S. Meyer, B. Dupé, R. Wiesendanger, K. von Bergmann, and S. Heinze, Phys. Rev. Lett. **120**, 207201 (2018).